Journal of Nuclear Materials 407 (2010) 2–9

Contents lists available at ScienceDirect

Journal of Nuclear Materials

journal homepage: www.elsevier.com/locate/jnucmat

Response of nanoclusters in a 9Cr ODS steel to 1 dpa, 525 °C proton irradiation

A.G. Certain [a,*], K.G. Field [a], T.R. Allen [a], M.K. Miller [b], J. Bentley [b], J.T. Busby [b]

[a] Material Science Program, University of Wisconsin, Madison, WI 53706, USA
[b] Materials Science and Technology Division, Oak Ridge National Laboratory, Oak Ridge, TN 37831, USA

A B S T R A C T

Ferritic–martensitic (F/M) alloys are expected to play an important role as cladding or structural components in Generation IV and other advanced nuclear systems operating in the temperature range 350–700 °C and to doses up to 200 displacements per atom (dpa). Oxide dispersion strengthened (ODS) F/M steels have been developed to operate at higher temperatures than traditional F/M steels. These steels contain nanometer-sized Y–Ti–O nanoclusters for additional strengthening. A proton irradiation to 1 dpa at 525 °C has been performed on a 9Cr ODS steel to determine the nanocluster stability at low dose. The evolution of the nanocluster population and the composition at the nanocluster–matrix interface were studied using electron microscopy and atom probe tomography. The data from this study are contrasted to those from a previous study on heavy-ion irradiated 9Cr ODS steel.

1. Introduction

Ferritic/martensitic (F/M) steels generally provide better swelling resistance under irradiation than austenitic steels, but have poor creep strength at temperatures over 600 °C [1]. Oxide dispersion strengthened (ODS) F/M 9Cr steels have been developed using the addition of nanoscale oxide particles to increase the high-temperature strength. These nanoclusters act as pinning points for dislocations, preserving the defect microstructure that helps give F/M steels their strength [2–4]. Since the nanoclusters give ODS steel its strength, the stability of the nanoclusters under irradiation is an important issue. Additionally, the nanoclusters are expected to promote recombination of irradiation-produced point defects and to trap transmutation-produced He in small, high-pressure bubbles [5]. This study combined the techniques of energy-filtered transmission electron microscopy (EFTEM) and atom probe tomography (APT) to study the effects of low-dose proton irradiation on the nanocluster population. To investigate changes in the local matrix composition that could affect the nanocluster stability through diffusion rather than ballistic damage, this study also used high spatial resolution energy-dispersive X-ray spectroscopy on a scanning transmission electron microscope (STEM/EDS) in conjunction with APT to investigate possible radiation-induced chromium segregation at the nanocluster–matrix interface.

2. Experimental

2.1. Specimen material

Two rod-shaped bulk specimens of 9Cr ODS ferritic steel measuring 24 mm in diameter and 60 mm in length, canned in mild steel, were provided by the Japan Nuclear Cycle Development Institute (now known as the Japan Atomic Energy Agency). The final heat treatment for the bulk specimens consisted of annealing at 1050 °C for 1 h and tempering at 800 °C for 1 h. The details of the fabrication, which is based on mechanical alloying (MA), have been described previously [2] and the compositions of the bulk specimens are given in Table 1. A bar specimen measuring 20 × 3 × 1 mm was cut from the bulk rod and was polished with 0.5 μm colloidal alumina prior to irradiation.

2.2. Irradiation (525 °C, 1 dpa, protons)

A Source of Negative Ions by Cesium Sputtering (SNICS) produced ions for the irradiation using a TiH cathode. The hydrogen ions were accelerated to 2.6 MeV by a National Electrostatics Corporation (NEC) Pelletron® tandem accelerator at the University of Wisconsin. The desired irradiation temperature of 525 °C was obtained through heating of the specimen by the beam alone. The temperature was monitored through three thermocouples connected to the stage, as well as observation of the stage with an infrared camera. The beam was rastered across the stage to achieve a uniform distribution of current over the specimen. Beam current and specimen temperature were recorded throughout the course of the irradiation through a National Instruments data acquisition

* Corresponding author.
E-mail address: acertain@wisc.edu (A.G. Certain).

0022-3115/$ - see front matter © 2010 Elsevier B.V. All rights reserved.
doi:10.1016/j.jnucmat.2010.07.002

Table 1
Target and measured composition of ODS steel received from Japan Atomic Energy Agency.

Target	Chemical composition (wt.%)													
	C	Si	Mn	P	S	Ni	Cr	W	Ti	Y	O	N	Ar	Fe
	0.13	–	–	–	–	–	9.0	2.0	0.22	0.275	0.20	–	–	Bal.
Bar 1	0.14	0.048	0.05	<0.005	0.003	0.06	8.60	1.95	0.23	0.28	0.14	0.017	0.004	Bal.
Bar 2	0.14	0.048	0.05	<0.005	0.004	0.06	8.67	1.96	0.23	0.27	0.14	0.017	0.004	Bal.

(DAQ) card. The temperature indicated by the thermocouples was kept within the range of 510–535 °C, and the damage rate in the metal matrix was $\sim 5 \times 10^{-6}$ dpa/s.

The damage rate of the ODS steel in this irradiation was calculated using SRIM 2006, stopping power version – 2003 [6]. Values of 40 eV were used for the displacement energy of both Fe and Cr. The protons used for the irradiation provided an almost flat damage profile ~20 μm deep, as can be seen from the SRIM damage rate profile in Fig. 1. Protons were chosen for this study for several reasons; irradiations with neutrons are usually more expensive, time consuming, and logistically complicated. Neutron-irradiated specimens have residual radioactivity after irradiation, and hence are more difficult and expensive to handle. Proton irradiations are low cost, leave specimens with little-to-no activity, and can achieve rapid damage rates [7]. The 9Cr ODS specimens were irradiated to nominally 1 dpa, measured using the calculated damage rate of the matrix.

2.3. Post-irradiation TEM sample preparation

Disks of 2.3 mm diameter were punched from the irradiated area of the ODS steel bar. Specimens for transmission electron microscopy (TEM) were electropolished using a 10% perchloric acid – 90% acetic acid solution and a current of 75 mA at room temperature. The material removal rate was determined by electropolishing multiple unirradiated 2.3 mm disk ODS steel specimens for 5-s periods. The specimens were imaged using a white-light interferometer; the depth between the outer rim that had been covered by a diaphragm and the lowest point of removal was measured. At the lowest point, where perforation would most likely occur, the removal rate was approximately 1 μm/s. The SRIM damage profile indicated that in the top ~20 μm of the sample surface the damage profile was almost flat, so the specimens were sectioned to ~5 μm from the irradiation surface by electropolishing for 5 s on the irradiated side. Electropolishing to perforation from the opposite side ensured that the thin area for TEM examination had been irradiated to a known dose. The specimens were slightly too thick for TEM after electropolishing and were Ar-ion-milled simultaneously from each side for 20 min at low voltage and 12° to the specimen surface using a Fischione 1010 ion mill. Unirradiated control specimens were similarly prepared, but were electropolished for an equal amount of time on each side to perforation.

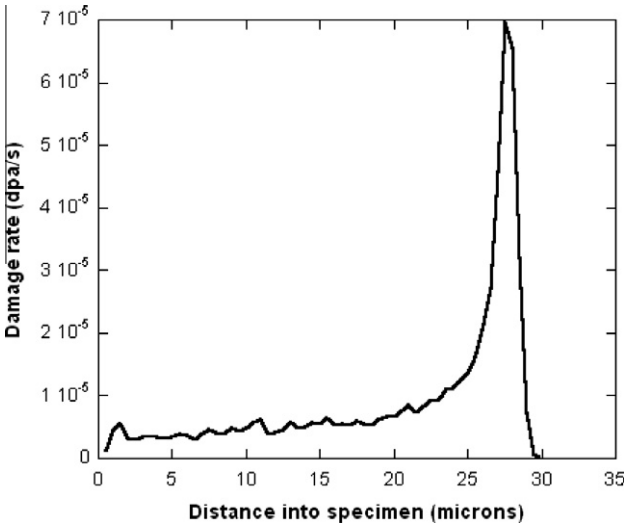

Fig. 1. SRIM damage rate profile for 9Cr steel bombarded with 2.6 MeV protons.

2.4. Energy-filtered transmission electron microscopy (EFTEM)

Imaging of nanoclusters by conventional TEM methods such as bright-field and dark-field diffraction contrast, through-focus phase-contrast imaging, and high-resolution TEM is unreliable, especially for nanoclusters <6 nm diameter [8]. Imaging by high-angle annular dark-field (HAADF) scanning transmission electron microscopy (STEM) has also proved unsatisfactory. However, energy-filtered TEM (EFTEM) can yield images that reliably reveal nanoclusters down to 2 nm diameter [8–10,5]. Energy-filtered images are formed by selecting a small range of inelastically scattered electrons with an energy-selecting slit in an imaging filter. This is achieved in practice by increasing the accelerating voltage of the microscope by the energy loss desired so that, after the corresponding energy loss events in the thin specimen, the mean energy of the electrons used for image formation is always the same.

Both 2-window and 3-window EFTEM methods [11] were used for this work. In the 3-window method, three images were recorded for each element, two with energy ranges below the ionization edge for a particular element, and one with an energy range immediately above the ionization edge. An extrapolated inverse power-law background image is calculated from the two pre-edge images and subtracted from the post-edge image to yield an elemental map. In the 2-window method, the post-edge image is divided by a pre-edge image to yield the jump-ratio image. The effects of non-uniform illumination, specimen thickness variations, and diffraction contrast are minimized in jump-ratio images. Although 3-window mapping using the FeL_{23} edge is possible, Fe–M jump-ratio images offer several advantages; the signal is much greater so smaller energy windows and shorter exposure times can be used leading to better resolution and less specimen drift [8]. It is not possible to produce Fe–M elemental maps reliably because the background shape precludes accurate extrapolation.

EFTEM was performed using a Philips CM30 operated at 300 kV and equipped with a LaB_6 cathode and a Gatan imaging filter (GIF). An incident beam convergence semi-angle $\alpha = 2.6$ mrad, a collection semi-angle $\beta = 4.8$ mrad, and doubly binned images of 512×512 pixels were used. Unirradiated samples and samples irradiated to 1 dpa at 525 °C of ODS steel were examined. Fe–M jump-ratio images were produced from typically 2-s exposures of component images recorded with 10-eV slits centered at energy losses of 46 and 62 eV; 3-window mapping of Ti–L_{23}, O–K, Cr–L_{23}, and C–K was performed with 30-eV slits. The overlap between O–K and Cr–L_{23} was overcome with 4-window processing [12]. Unfiltered and zero-loss (10 eV slit) images were also recorded and used to create a thickness map based on the relationship:

$$\frac{t}{\lambda} = \ln\frac{I_T}{I_0} \quad (1)$$

where t is the thickness of the sample, λ is the inelastic scattering mean free path length (~140 nm for the compositions and conditions used in this work), I_T is the unfiltered image and I_0 is the zero-loss filtered image. Fe–M jump-ratio images were used for nanocluster size measurements and, in conjunction with the thickness maps, for nanocluster number–density measurements. Nanoclusters under ~2 nm were not visible using this technique even for $t < 40$ nm.

2.5. Scanning transmission electron microscopy/energy-dispersive X-ray spectroscopy (STEM/EDS)

Irradiated and unirradiated specimens were characterized by STEM/EDS. Composition profiles were measured at ORNL using a Philips CM200/-FEG TEM–STEM operated at 200 kV in the STEM mode. Drift-corrected spectrum-profiles (line scans) were acquired across grain boundaries and nanoclusters using an incident probe of ~1.5 nm full-width at half-maximum (FWHM), a pixel spacing of 1.5 nm and a dwell (acquisition time) of 15 s/pixel.

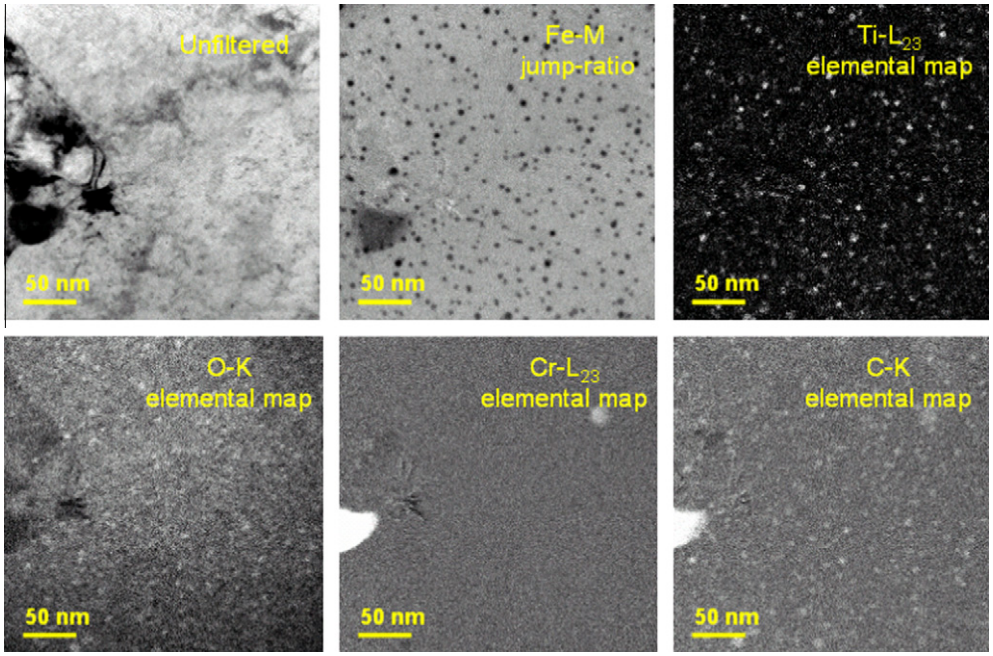

Fig. 2. EFTEM images of a typical region in unirradiated material. Ti enrichment corresponds to areas of Fe depletion with the exception of the large area of Fe depletion at the left. The Cr and C maps indicate that this area is chromium carbide. The other smaller chromium carbide towards the top-right is on the specimen surface since it does not exhibit Fe depletion.

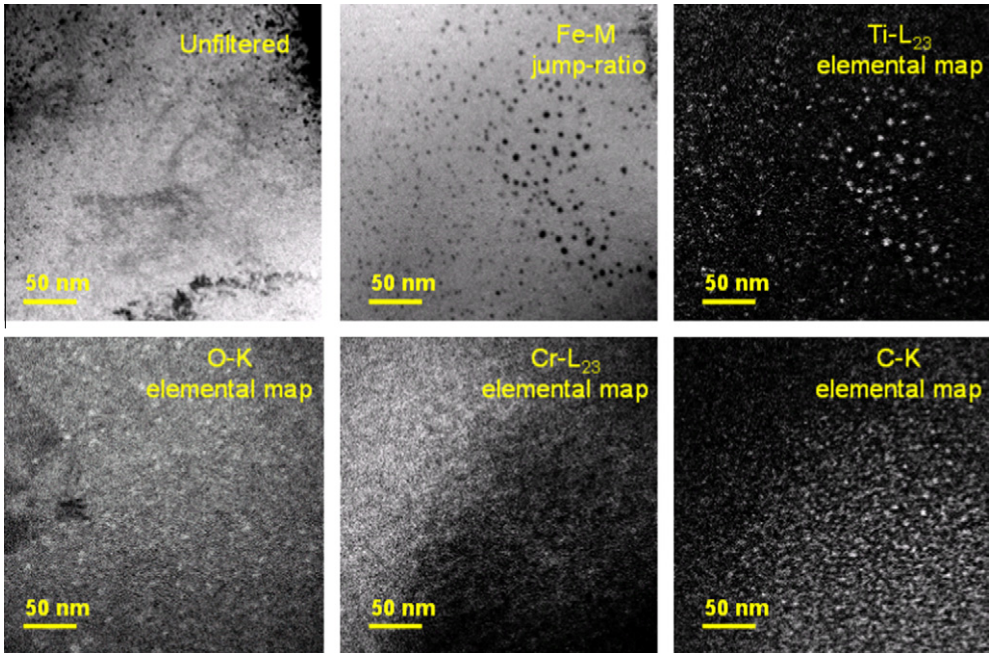

Fig. 3. Set of EFTEM images for ODS irradiated to 1 dpa at 525 °C.

2.6. Atom probe tomography (APT)

APT is used as a complimentary technique to EFTEM, as it can resolve nanoclusters sized than 2 nm in diameter. Specimens for APT were prepared from the unirradiated and irradiated materials using an FEI Nova 200 focused ion beam (FIB) instrument. A 3 μm × 10 μm × 6 μm wedge was lifted from the bulk and then annular milled to form a sharp needle [13]. The specimens were characterized with an Imago Scientific Instruments local electrode atom probe (LEAP) at ORNL. A specimen temperature of 60 K, a pulse repetition rate of 200 kHz and a pulse fraction of 0.2 were used for the analyses. Nanoclusters were located in the samples by searching the three-dimensional data for Ti and O solute atoms that were within a certain distance of another solute atom of the same type [14]. This maximum separation (a friends-of-friends) [15] method enables the solutes in the nanoclusters to be distinguished from the solutes in the matrix so that the size, composition, and number density of the nanoclusters can be estimated. The maximum separation distance depends on the solute concentrations in the nanoclusters and the matrix. A maximum separation distance of 0.6 nm was used in this study. This method detects solute agglomerations containing two or more atoms of interest. As some of the smaller agglomerations are due to the solute distribution in a random solid solution, a minimum size limit of 10 atoms was used to eliminate these regions. The center-of-mass, the radius of gyration, l_g, and the Guinier radius, r_G, were estimated directly from the coordinates of the solute oxygen atoms in each nanocluster [16]. The number density, N_v, was estimated from the number of nanoclusters in the analyzed volume, which in turn was estimated from the total number of atoms in the volume, their atomic volumes, and an assumed detector efficiency [16].

3. Results

3.1. EFTEM

In the Fe–M jump-ratio images, areas of Fe depletion are clearly visible. When compared to the Ti–L elemental maps, the areas depleted in Fe correlate with areas of Ti enrichment, as shown in Fig. 2 which shows EFTEM images for a region of unirradiated material. The small image features exhibiting Fe depletion and Ti enrichment are the Y-, Ti- and O-enriched nanoclusters previously observed by EFTEM and APT in MA/ODS 12YWT, 14YWT and MA957 nanostructured ferritic alloys (NFA) [16–21]. Yttrium is difficult to image using EFTEM, especially at low effective concentration; the Y–M_{45} edge (~157 eV) has a delayed maximum and background fitting is complicated by non-power-law behavior, the Y–L_3 edge (>2 keV) provides only a weak signal, and the Y–N_{23} edge (~26 eV) is compromised by plasmon excitation. Most of the oxygen elemental maps and jump-ratio images were inconclusive due to surface oxidation, although some showed correlation with the nanoclusters. Carbon elemental maps indicated that many of the larger (>20 nm) regions depleted in Fe had a strong carbon signal, so were consistent with Cr or Ti carbides depending on corresponding enrichment indicated in Cr or Ti elemental maps. Carbon elemental maps indicated that the nanoclusters had slight C enrichment in both the unirradiated and irradiated conditions, in agreement with previous atom probe work on alloy 14YWT [20].

EFTEM images for a region in the irradiated material are shown in Fig. 3, including an unfiltered image (equivalent to a conventional bright-field image) for comparison. The bright-field image clearly illustrates that the nanoclusters are not easily identified using conventional bright-field TEM imaging due to diffraction contrast from defects, bend contours, and the low contrast between the nanoclusters and the matrix. The nanocluster distribution is heterogeneous, and hence the number density varied widely between areas examined, as illustrated in Fig. 4. The diameter and number density results are shown in Table 2. Histograms of the nanocluster size distributions compiled from all of the areas sampled are shown in Fig. 5. Approximately 2000 nanoclusters were measured for each specimen.

3.2. STEM/EDS

Not enough information about the nanocluster composition is known yet to deconvolute the intensities of the data taken from individual nanoclusters. Unlike grain boundaries in TEM samples, which frequently run all the way through the thickness of the sample, an unknown thickness of matrix material exists above and below the analyzed nanoclusters. A schematic of the condition of the

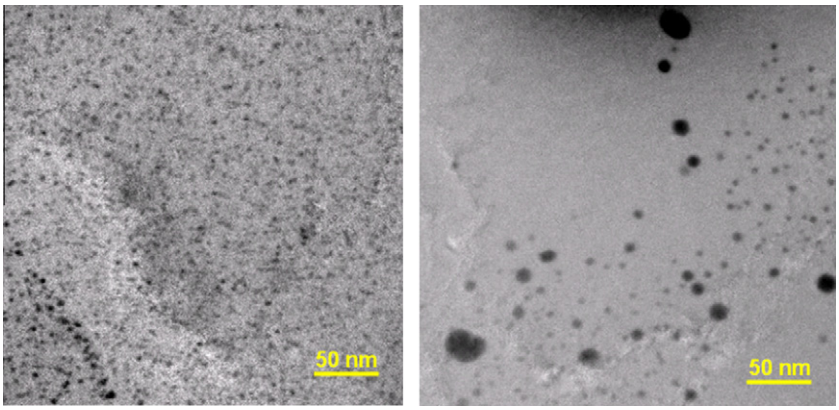

Fig. 4. Fe–M jump-ratio images from different areas of the irradiated specimen showing differences in nanocluster distribution.

Table 2
Size and number density statistics from EFTEM analysis of nanoclusters.

	Mean size (nm)	Standard deviation (nm)	Standard deviation of the mean (nm)	Mean number density (nanoclusters/nm^3)	Standard deviation (nanoclusters/nm^3)	Standard deviation of the mean (nanoclusters/nm^3)
Unirradiated	3.4	1.8	0.1	9.40×10^{-5}	4.1×10^{-5}	1.70×10^{-5}
Irradiated 1 dpa, 525 °C	3.1	2	0.1	1.18×10^{-4}	8.20×10^{-5}	8.40×10^{-5}

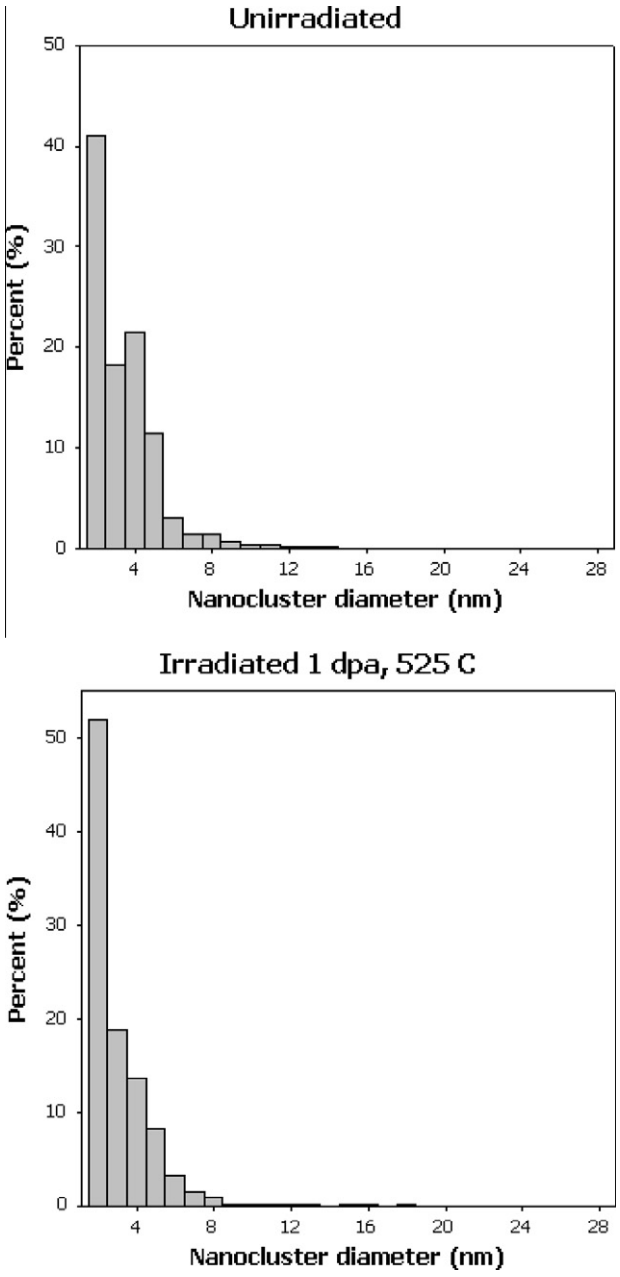

Fig. 5. Histograms of nanocluster sizes compiled from all unirradiated and irradiated sampled areas. The unirradiated specimen had nanoclusters as large as 28 nm, the irradiated specimen had nanoclusters as large as 25 nm. The incidence of these particles was so low that they are not visible on the histogram.

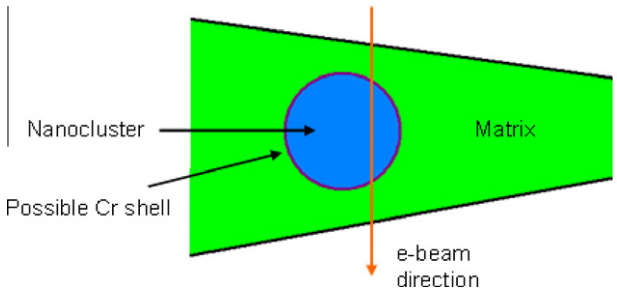

Fig. 6. Cartoon of sample geometry for STEM/EDS analyses. The X-ray excitation volume includes both matrix and nanocluster.

sample volume analyzed is shown in Fig. 6. The unknown amount of matrix material contributing to the profiles will skew the concentrations of Fe and Cr. The raw EDS intensity profiles for several of the nanoclusters show a slight Cr peak at what is considered to be the edge of the nanocluster based on the Y and Ti intensities; an example of a compositional plot from an irradiated sample that has these peaks in Cr intensity is shown in Fig. 7. These same peaks were not seen in profiles for nanoclusters in the unirradiated specimen. This might indicate radiation-induced segregation of Cr at the nanocluster–matrix interface, but as will be discussed, this same enrichment is not seen in the APT measurements. Approximately 10 nanoclusters were analyzed for each condition, with around half of the irradiated clusters showing the segregation effect. The scans that did not show the effect were too noisy to detect a subtle increase in Cr concentration.

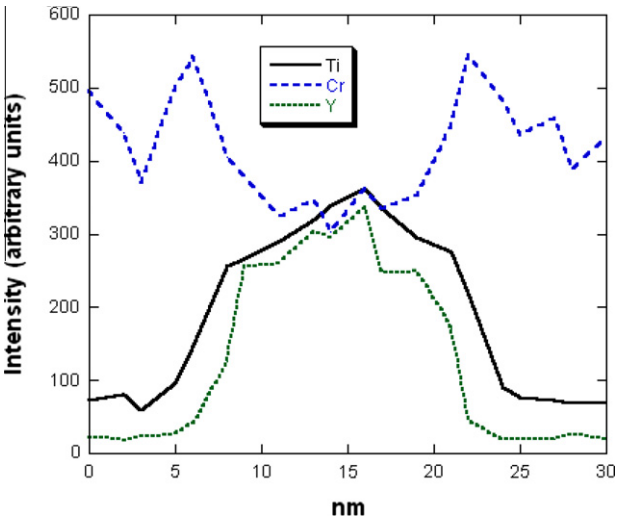

Fig. 7. STEM/EDS line scan data taken across a nanocluster of ~15 nm diameter in a specimen irradiated to 1 dpa at 525 °C. Due to complicated sample geometry, the raw data is presented in intensity rather than concentration. Peaks in Cr intensity are observed at the edge of the nanoclusters.

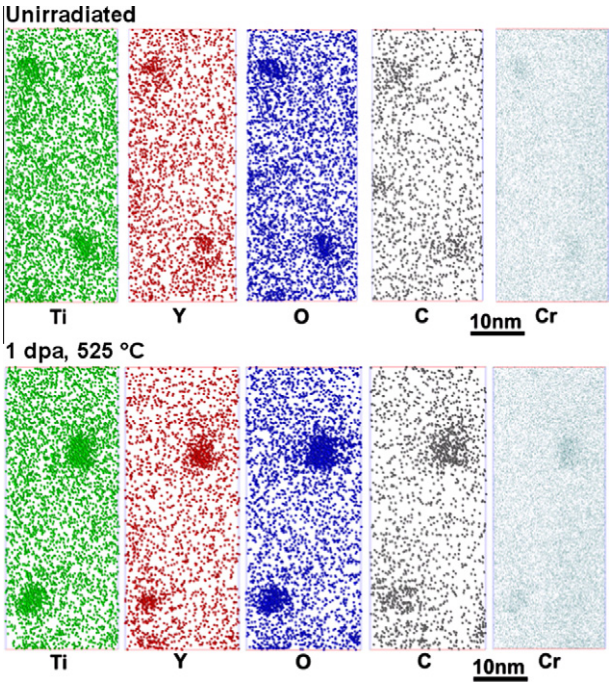

Fig. 8. APT atom maps from the specimen irradiated to1 dpa at 525 °C.

3.3. APT

APT atom distribution maps revealed the presence of Ti-, Y- and O-enriched nanoclusters in the matrix of both the unirradiated and irradiated samples, as shown in Fig. 8. The average Guinier radius, r_G, and number density N_v for the unirradiated and irradiated specimens are shown in Table 3. Elemental segregation at the surface of the nanoclusters was investigated by assembling a proximity histogram [22]. An isoconcentration surface was constructed for the nanoclusters as seen in Fig. 9, and the shortest distance of each atom to the nearest isoconcentration surface was determined and the identity of the solute atom was accumulated into a data bin representing that distance from the interface. The data for all of the nanoclusters in the same sample volume were combined to reduce statistical errors, and the solute concentrations were then plotted as a function of distance from the isoconcentration surface, as seen in Fig. 10. Approximately 50 nanoclusters from the unirradiated sample and ~100 nanoclusters from the irradiated sample were used for the size measurements, number-density measurements, and proximity histograms.

Table 3
Size and number-density measurements from APT.

	Guinier radius, r_G (nm)	Nanocluster density, N_v (nanoclusters/nm^3)
Unirradiated	0.97	9.86E−04
Irradiated 1 dpa, 525 °C	1.09	8.45E−04

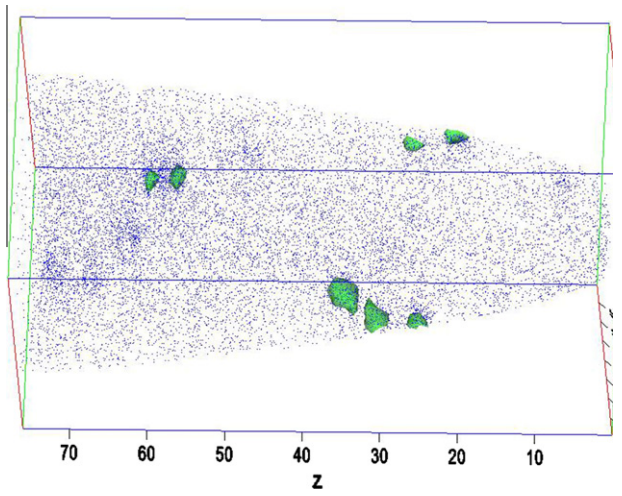

Fig. 9. Atom map of the 1 dpa, 525 °C irradiated specimen with isoconcentration surfaces added to represent the nanocluster boundaries. *Z* is in nm.

4. Discussion

4.1. Bright-field TEM versus EFTEM

A previous study on this material used bright-field (BF) TEM images to measure the nanocluster sizes on an unirradiated specimen and specimens irradiated to 5, 50, and 150 dpa with Ni-ions [23]. The EFTEM data from the present study measured a much smaller nanocluster average diameter for the unirradiated material: 11.7 nm for the BF study, 3.35 nm for the EFTEM study, as well as a more positive skewness for the size distribution: +1.5 for the BF study and +3.4 for the EFTEM study. The larger positive skewness in the EFTEM data indicates the measured mean is located at a smaller size compared to the measured mean that is seen in the BF TEM measurements. Since the number of large particles measured is comparable with both techniques, this greater skewness indicates that EFTEM is more effective than BF TEM for detecting smaller-sized nanoclusters. The BF TEM study reported that around half of the observed nanocluster volume disappeared (became smaller than the resolution of the BF TEM imaging technique) under irradiation at temperatures of 600 °C and 700 °C, but a comparable loss was not seen for 500 °C irradiations. No change in observed nanocluster volume was found in the current EFTEM study for irradiation at 525 °C. The BF TEM study also reported only one number density for the unirradiated specimen and each irradiated condition. The spread of number densities discussed in the next section indicates that the alloy is too inhomogeneous to accurately be described by a single value.

4.2. Inhomogeneous nanocluster distribution

The number densities obtained through EFTEM do not indicate a homogeneous distribution of nanoclusters. The scatter plots seen in Fig. 11 demonstrate the wide range in nanocluster number density from area to area, as well as a negative correlation with the average size measured in the area. Changes in the particle population due to irradiation can only be quantified by comparing the spread of number densities observed in the samples, rather than a single average value. There was no correlation found between number density and the thickness of the area being sampled.

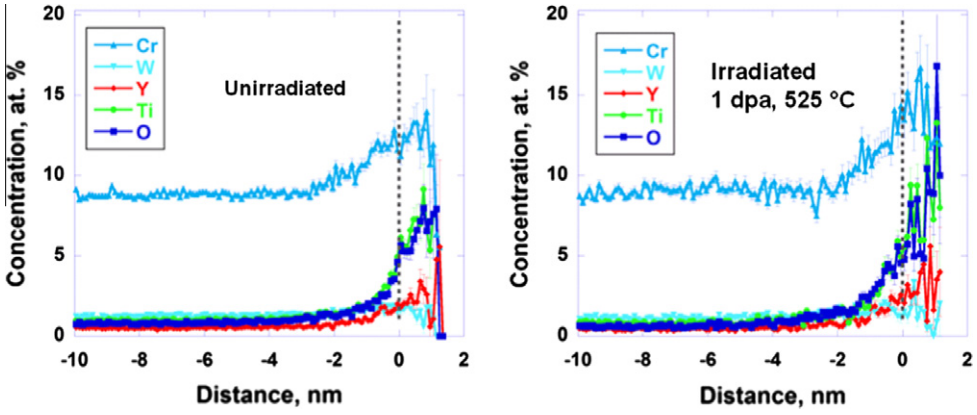

Fig. 10. Proximity histograms including all nanoclusters in each sample.

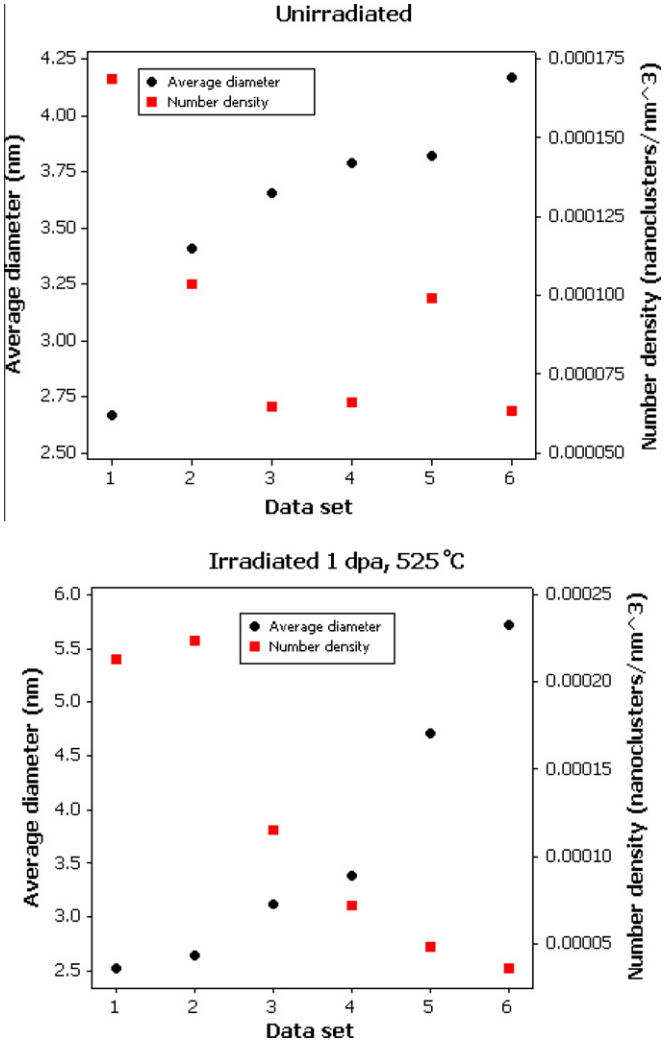

Fig. 11. Average diameter and number densities for nanoclusters measured using EFTEM from different areas of the specimens, revealing negatively correlated ranges of values.

4.3. EFTEM and APT

EFTEM showed a wide range of nanocluster sizes, mostly within the range of 2–10 nm in diameter, but also a limited number of nanoclusters that were >10 nm. There was a cut-off size of ~2 nm, below which nanoclusters were not detectable by the EFTEM technique. APT was able to reveal nanoclusters less than 2 nm in diameter. Since the material is heterogeneous, EFTEM found a larger range of nanocluster sizes is found using EFTEM by sampling more material: $\sim 2 \times 10^7$ nm^3 of each specimen is analyzed by EFTEM, while $\sim 5 \times 10^4$ nm^3 is analyzed by APT. However, the smallest nanoclusters were founding using APT, which could not be detected by EFTEM. If the size distribution and number density results from APT are scaled up to the volumes analyzed by EFTEM assuming the material is homogeneous, it would be expected to see approximately a 10-fold increase in the number of nanoclusters detected. Although the material is not homogeneous, as shown by previous APT studies and as revealed in the present EFTEM results, even a fraction of this increase indicates that nanoclusters <2 nm diameter detected by APT are a substantial part of the population. The average size measured from the EFTEM data is larger than that measured from the APT data, while the true average probably lies somewhere in between. The nanocluster population cannot be fully described by either method alone; these techniques should be viewed as complementary to each other.

4.4. Radiation effects

The nanocluster size distributions of data compiled from all areas sampled using EFTEM for the unirradiated and irradiated material had similar shapes. The average size in the irradiated sample was slightly smaller than that in the unirradiated material (3.1 nm compared to 3.4 nm, or a decrease in diameter of −0.3 nm/dpa). A similar effect was reported in the BF TEM studies of material irradiated at 500 °C–5 dpa (10.5 nm after 5 dpa as compared to 11.7 nm in the unirradiated samples, a similar decrease in diameter of −0.24 nm/dpa) [23]. Statistical analysis of the nanocluster size distributions measured from EFTEM maps revealed a distribution heavily skewed towards smaller sizes: the distributions had skewness values of +3.40 with a 0.05 standard error and +4.15 with a 0.06 standard error for the unirradiated and irradiated conditions, respectively. Additional higher-dose data is needed, but initial indications are consistent with the previous Ni-ion irradiations in that size distributions tend towards the smaller-sized nanoclusters. The distributions are also more peaked than a normal distribution, with a kurtosis value of +25.79 with a standard error of 0.10 for the unirradiated sample and +28.05 with a standard error of 0.11 for the irradiated sample. The average size and number density were similar for the APT samples of unirradiated and irradiated material, indicating that the nanoclusters are stable, but since only one sample from each is being compared it is not known whether or not the smaller nanocluster population has a heterogeneous distribution similar to the larger nanoclusters.

The EFTEM data for the irradiated specimen showed a broader range of number densities than the data for the unirradiated specimen and also showed areas of higher number density. When the nanocluster sizes are compared within a narrow range of sizes (i.e. comparing 2–3 nm diameter data, then 2–4 nm, etc. between the unirradiated and irradiated cases) the difference in the average size within each size range bin increases for the larger sizes. This indicates that poor statistical sampling, as well as any possible radiation effect, may contribute to differences in reported average nanocluster sizes; additional irradiation conditions are required for a more complete examination of the radiation stability.

The APT proximity histogram results show that rather than radiation-induced segregation of Cr to the matrix–nanocluster interface indicated by the STEM/EDS, the nanoclusters themselves are chromium enriched in both the unirradiated and irradiated condition.

5. Conclusions

EFTEM and APT were found to be complementary techniques for detecting the range of nanocluster sizes in ODS steel. A range of number densities was observed from area to area on the specimens using EFTEM, which was inversely proportional to the average size of the nanoclusters observed in the respective areas. The EFTEM technique proved to be a better approach to detect smaller nanoclusters than the BF TEM imaging used in previously published studies. The nanoclusters were shown to be stable using APT and higher-dose data is needed to confirm trends from EFTEM data. Irradiation effects on nanoclusters at different temperatures will also be evaluated in future work; simple radiation induced ballistic dissolution will lead to a linear loss rate with respect to dose, but if diffusion effects are significant to dissolution the results will be more complex.

APT data showed that the nanoclusters were enriched with chromium in both the unirradiated and irradiated specimens, but did not show radiation-induced segregation of chromium to

the nanocluster–matrix interface that was indicated in STEM/EDS measurements. If radiation-induced diffusion of point defects is critical to the oxide dissolution, then a radiation-induced segregation profile is expected at the surface of the nanocluster; future work will continue to evaluate whether any radiation-induced segregation is occurring.

Acknowledgments

STEM/EDS, EFTEM and APT research at Oak Ridge National Laboratory was sponsored by the Division of Materials Sciences and Engineering, Office of Basic Energy Sciences, by the Advanced Fuel Cycle Initiative, Office of Nuclear Energy, Science and Technology, and at the SHaRE User Facility sponsored by the Division of Scientific User Facilities, Office of Basic Energy Sciences, US Department of Energy. The ODS sample material was generously provided by the Japan Atomic Energy Agency.

References

[1] F.A. Garner, M.B. Toloczko, B.H. Sencer, J. Nucl. Mater. 276 (2000) 123–142.
[2] S. Ohtsuka, S. Ukai, M. Fujiwara, T. Kaito, Mater. Trans. 46 (3) (2005) 487–492.
[3] H. Sakasegawa, S. Ukai, M. Tamura, S. Ohtsuka, H. Tanigawa, H. Ogiwara, et al., J. Nucl. Mater. 373 (1–3) (2008) 82–89.
[4] S. Ukai, T. Okuda, M. Fujiwara, T. Kobayashi, S. Mizuta, J. Nucl. Sci. Technol. 39 (8) (2002) 872–879.
[5] T. Yamamoto, G.R. Odette, P. Miao, D.T. Hoelzer, J. Bentley, N. Hashimoto, H. Tanigawa, R.J. Kurtz, J. Nucl. Mater. 367–370 (2007) 399–410.
[6] J.F. Ziegler, J.P. Biersack, SRIM 2006, Yorktown, NY, 2006.
[7] G.S. Was, J.T. Busby, T.R. Allen, E.A. Kenik, A. Jenssen, S.M. Bruemmer, et al., J. Nucl. Mater. 300 (2–3) (2002) 198–216.
[8] J. Bentley, D.T. Hoelzer, D.W. Coffey, K.A. Yarborough, Microsc. Microanal. 10 (Suppl 2) (2004) 662.
[9] J. Bentley, D.T. Hoelzer, H. Tanigawa, T. Yamamoto, G.R. Odette, Microsc. Microanal. 13 (Suppl 2) (2007) 1072.
[10] J. Bentley, D.T. Hoelzer, Microsc. Microanal. 14 (Suppl 2) (2008) 1416.
[11] L. Reimer, Electron Spectroscopic Imaging, Springer, 1995.
[12] J. Bentley, Microsc. Microanal. 6 (Suppl. 2) (2000) 1186.
[13] M.K. Miller, K.F. Russell, K. Thompson, R. Alvis, Microsc. Microanal. 13 (6) (2007) 428–436.
[14] J.M. Hyde, C.A. English, Microstructural processes in irradiated materials – 2000, in: Symposium (Mater. Res. Soc. Proceedings), vol. 650, 2001, p. 6.
[15] J.P. Huchra, Astrophys. J. 257 (2) (1982) 423–437.
[16] M.K. Miller, Atom Probe Tomography: Analysis at the Atomic Level, Kluwer Academic/Plenum Publishers, NY, 2000.
[17] M.K. Miller, E.A. Kenik, K.F. Russell, L. Heatherly, D.T. Hoelzer, Mater. Sci. Eng. A – Struct. A353 (1–2) (2003) 140–145.
[18] M.K. Miller, D.T. Hoelzer, E.A. Kenik, K.F. Russell, in: Proceedings of the 11th Conference on Fusion Research, vol. 329–333(1–3), 2004, pp. 338–341.
[19] M.K. Miller, D.T. Hoelzer, E.A. Kenik, K.F. Russell, Intermetallics 13 (3–4) (2005) 387–392.
[20] M.K. Miller, K.F. Russell, J. Nucl. Mater. 351 (1–3) (2006) 261–268.
[21] S. Yamashita, K. Oka, S. Ohnuki, N. Akasaka, S. Ukai, J. Nucl. Mater. 307–311 (1) (2002) 283–288.
[22] O.C. Hellman, J.A. Vandenbroucke, J. Rusing, D. Isheim, D.N. Seidman, Microsc. Microanal. 6 (5) (2000) 437–444.
[23] T.R. Allen, J. Gan, J.I. Cole, M.K. Miller, J.T. Busby, S. Shutthanandan, S. Thevuthasan, et al., J. Nucl. Mater. 375 (1) (2008) 26–37.